

Simulating the impact of HI fluctuations on matched filter search for ionized bubbles in redshifted 21 cm maps

Kanan K. Datta^{1*}, Suman Majumdar^{1†}, Somnath Bharadwaj^{1‡} and T. Roy Choudhury^{2§}

¹*Department of Physics and Meteorology & Centre for Theoretical Studies, IIT, Kharagpur 721302, India*

²*Institute of Astronomy, Madingley Road, Cambridge CB3 0HA, UK*

1 November 2018

ABSTRACT

Extending the formalism of Datta, Bharadwaj & Choudhury (2007) for detecting ionized bubbles in redshifted 21 cm maps using a matched-filtering technique, we use different simulations to analyze the impact of HI fluctuations outside the bubble on the detectability of the bubble. In the first three kinds of simulations there is a spherical bubble of comoving radius R_b , the one that we are trying to detect, located at the center, and the neutral hydrogen (HI) outside the bubble traces the underlying dark matter distribution. We consider three different possible scenarios of reionization, i.e., (i) there is a single bubble (SB) in the field of view (FoV) and the hydrogen neutral fraction is constant outside this bubble (ii) patchy reionization with many small ionized bubbles in the FoV (PR1) and (iii) many spherical ionized bubbles of the same radius R_b (PR2). The centers of the extra bubbles trace the dark matter distribution. The fourth kind of simulation uses more realistic maps based on semi-numeric modelling (SM) of ionized regions. We make predictions for the currently functioning GMRT and a forthcoming instrument, the MWA at a redshift of 6 (corresponding to a observed frequency 203 MHz) for 1000 hrs observations. We find that for both the SB and PR1 scenarios the fluctuating IGM restricts bubble detection to size $R_b \leq 6$ Mpc and $R_b \leq 12$ Mpc for the GMRT and the MWA respectively, however large be the integration time. These results are well explained by analytical predictions. In the PR2 scenario, we find that bubble detection is almost impossible for neutral fraction $x_{\text{HI}} < 0.6$ because of large uncertainty due to the HI fluctuations. Applying the matched-filter technique to the SM scenario, we find that it works well even when the targeted ionized bubble is non-spherical due to surrounding bubbles and inhomogeneous recombination. We find that determining the size and positions of the bubbles is not limited by the HI fluctuations in the SB and PR1 scenario but limited by the instrument’s angular resolution instead, and this can be done more precisely for larger bubble. We also find that for bubble detection the GMRT configuration is somewhat superior to the proposed MWA.

Key words: cosmology: theory, cosmology: diffuse radiation, Methods: data analysis

1 INTRODUCTION

The epoch of reionization is one of the least known chapters in the evolutionary history of the Universe. Quasar absorption spectra (Becker et al., 2001; Fan et al., 2002, 2006a) and CMBR observations (Spergel et al., 2006; Page et al., 2006; Dunkley et al., 2008) together imply that reionization occurred over an extended period spanning the redshift range $6 \leq z \leq 15$ (for reviews see Fan, Carilli & Keating 2006; Choudhury & Ferrara 2006). It is believed that the ionizing radiation from quasars and the stars within galax-

ies reionize the surrounding neutral intergalactic medium (IGM). Ionized bubbles form around these luminous objects, grow and finally overlap to completely reionize the Universe. The issue of detecting these bubbles in radio-interferometric observations of redshifted HI 21 cm radiation has been drawing considerable attention. This is motivated by the Giant Metre-Wave Radio Telescope (GMRT¹; Swarup et al. 1991) which is currently functional and several low frequency radio telescopes which are expected to become functional in the future (eg. MWA², LOFAR³, 21 CMA⁴,

* E-mail: kanan@cts.iitkgp.ernet.in

† E-mail: sumanl@cts.iitkgp.ernet.in

‡ E-mail: somnathb@iitkgp.ac.in

§ E-mail: chou@ast.cam.ac.uk

¹ <http://www.gmrt.ncra.tifr.res.in>

² <http://www.haystack.mit.edu/ast/arrays/mwa/>

³ <http://www.lofar.org/>

⁴ <http://web.phys.cmu.edu/~past/>

PAPER⁵, VLA extension program⁶ and SKA⁷). These are all being designed to be sensitive to the HI signal from the epoch of reionization.

The detection of individual ionized bubbles would be a direct probe of the reionization process. It has been proposed that such observations will probe the properties of the ionizing sources and the evolution of the surrounding IGM (Wyithe & Loeb, 2004a; Wyithe, Loeb & Barnes, 2005; Kohler et al., 2005; Maselli et al., 2007; Alvarez & Abel, 2007; Geil & Wyithe, 2008; Wyithe, 2008; Geil et al., 2008). Observations of individual ionized bubbles would complement the study of reionization through the power spectrum of HI brightness temperature fluctuations (Zaldarriaga, Furlanetto & Hernquist, 2004; Morales & Hewitt, 2004; Bharadwaj & Ali, 2005; Ali, Bharadwaj & Pandey, 2005; Sethi, 2005; Datta, Choudhury & Bharadwaj, 2007).

Nearly all the previous work on detecting ionized regions consider the contrast between the ionized regions and the neutral IGM in images of redshifted HI 21 cm radiation. The HI signal is expected to be only a small contribution buried deep in the emission from other astrophysical sources (foregrounds) and in the system noise. It is a big challenge to detect the signal of an ionized bubble from the other contributions that are orders of magnitude larger (Shaver et al., 1999; Di Matteo et al., 2002; Oh & Mack, 2003; Cooray & Furlanetto, 2004; Santos, Cooray & Knox, 2005; Gleser et al., 2007; Ali et al., 2008). In an earlier work (Datta, Bharadwaj & Choudhury 2007, hereafter referred to as Paper I) we have introduced a matched filter to optimally combine the entire signal of an ionized bubble while minimizing the noise and foreground contributions. This technique uses the visibilities which are the fundamental quantity measured in radio-interferometric observations. Using visibilities has an advantage over the image based techniques because the system noise contribution in different visibilities is independent whereas the noise in different pixels of a radio-interferometric images is not.

Paper I presents an analytic framework for predicting the expected value and the standard deviation σ of the matched filter estimator for the detection of a spherical ionized bubble of comoving radius R_b . We identify three different contributions to σ , namely foregrounds, system noise and the fluctuations in the HI outside the bubble that we are trying to detect. Our analysis shows that the matched filter effectively removes the foreground contribution so that it falls below the signal. Considering the system noise for the GMRT and the MWA we find that a 3σ detection will be possible for a bubble of comoving radius $R_b \geq 40$ Mpc in 100 hrs of observation and $R_b \geq 22$ Mpc in 1000 hrs of observation for both the instruments. The HI fluctuations, we find, impose a fundamental restriction on bubble detection. Under the assumption that the HI outside the ionized bubble traces the dark matter we find that it is not possible to detect bubble of size $R_b \leq 8$ Mpc and $R_b \leq 16$ Mpc at the GMRT and MWA respectively. Note that the matched filter technique is valid for both, a targeted search around QSOs as well as for a blind search in a random direction.

In this paper we validate the visibility based matched filter technique introduced in Paper I through simulations of bubble detection. Our simulations are capable of handling interferometric arrays with widely different configurations like the GMRT and the MWA, the two instruments that we consider here. As mentioned

earlier, the fluctuations in the HI outside the target bubble impose a fundamental restriction for bubble detection. The analytic approach of Paper I assumes that the HI outside the bubble traces the dark matter. In this paper we carry out simulations that incorporate this assumption and use these to assess the impact of HI fluctuations for bubble detection. We also use the simulations to determine the accuracy to which the GMRT and the MWA will be able to determine the size and the position of an ionized bubble, and test if this is limited due to the presence of HI fluctuations. In a real situation a typical FoV is expected to contain several ionized patches besides the one that we are trying to detect. We use simulations to assess the impact of HI fluctuations for bubble detection in patchy reionization scenarios.

The outline of the paper is as follows. Section 2 presents a brief description of how we simulate 21-cm maps for three different scenarios of the HI distribution, one where the HI traces the dark matter and two with patchy reionization. Subsections 2.1 and 2.2 respectively discuss how the simulated maps are converted into visibilities and how the matched filter analysis is simulated. We present our results in Section 3. Subsections 3.1, 3.2 and 3.3 present results for bubble detectability, size determination and position determination under the assumption that the HI outside the bubble traces the dark matter. Section 3.4 presents results for bubble detectability in patchy reionization scenarios. We discuss redshift dependence of bubble detection in section 4 and present our summary in section 5.

For the GMRT we have used the telescope parameters from their website, while for the MWA we use the telescope parameters from Bowman et al. (2007). The cosmological parameters used throughout this paper are $\Omega_m = 0.3$, $\Omega_b h^2 = 0.022$, $n_s = 1.$, $h = 0.74$, $\sigma_8 = 1$.

2 METHOD OF SIMULATION

We have simulated the detection of the HI signal of an ionized bubble whose center is at redshift $z_c = 6$ which corresponds to $\nu_c = 203$ MHz. The choice of z value is guided by the fact that we expect large ionized regions towards the end of reionization $z \gtrsim 6$ (Wyithe & Loeb, 2004b; Furlanetto et al., 2006). Our aim here is to validate the analytic calculations of Paper I and hence the exact value of z is not very important.

We consider four scenarios of reionization for bubble detection. In the first three scenarios there is a spherical ionized bubble, the one that we are trying to detect, at the center of the FoV. This bubble has comoving radius R_b and is embedded in HI that traces the dark matter. In the first scenario there is a single bubble in the field of view. We refer to this as the SB scenario. In this scenario the HI fraction x_{HI} is assumed to be uniform outside the bubble. The uncertainty due to the HI fluctuations is expected to be lowest in this scenario because of the absence of patchiness. This is the most optimistic scenario for bubble detection.

In the next two scenarios, we attempt to quantify the effect of patchy reionization (PR) outside the bubble that we are trying to detect by introducing many other, possibly overlapping, bubbles in the FoV. Unfortunately, there is no obvious way to fix the sizes of these bubbles from any theoretical models as they depend crucially on the nature of reionization sources and other physical factors. In scenario PR1, we assume that the large HII regions which we are trying to detect are surrounded by many small ionized regions whose sizes are fixed by the following procedure: we assume the globally averaged neutral fraction x_{HI} to be ~ 0.5 ; the reason for

⁵ <http://astro.berkeley.edu/~dbacker/eor/>

⁶ <http://www.cfa.harvard.edu/dawn/>

⁷ <http://www.skatelescope.org/>

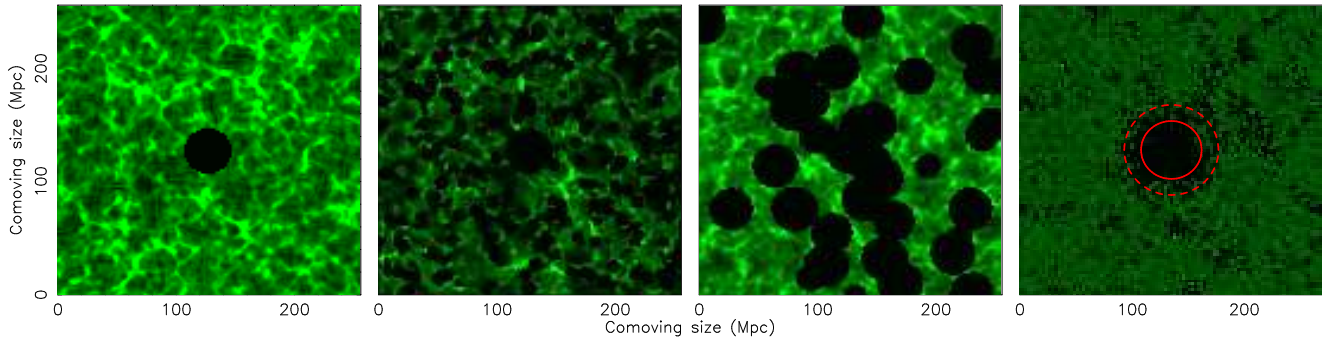


Figure 1. This shows HI images on slices through the center of the bubble for the four different scenarios SB, PR1, PR2 and SM (from left to right). In first three panels the central, circular dark region of radius $R_b = 20$ Mpc shows the HII bubble that we are trying to detect. The HI outside this bubble traces the dark matter distribution. In the SB scenario (left) the hydrogen neutral fraction is $x_{\text{HI}} = 1$ outside the bubble. In the PR1 scenario (2nd from left) the extra bubbles are all of a fixed comoving radius 6 Mpc. In the PR2 scenario (3rd from left) the extra bubbles have the same comoving radius as the bubble that we are trying to detect. In both the PR1 and PR2 reionization scenarios the centers of the extra bubbles trace the dark matter distribution and $x_{\text{HI}} = 0.62$. In the SM scenario (right) the central region up to radius 27 Mpc is fully ionized (marked with solid circle) and beyond that region up to radius 42 Mpc the region is partially filled with HI patches (dashed circle). The mean neutral fraction is $x_{\text{HI}} = 0.5$. These simulations are all for the GMRT.

this choice is that the effects of patchiness would be most prominent when typically half of the IGM is ionized. Given the value of x_{HI} , we try to obtain a reasonable estimate of the size of the background bubbles from available models. For example, semi-numeric simulations of patchy reionization (Mesinger & Furlanetto, 2007) predict that the bubble size distribution peaks around 5 Mpc when $x_{\text{HI}} = 0.61$ (see their Fig 6). We thus choose the spherical background bubbles to have radii 6 Mpc and compute the number of background bubbles by demanding that the resulting neutral fraction is 0.5. The bubble centres are chosen such that they trace the underlying dark matter distribution. At the end, the value of x_{HI} turns out to be slightly higher 0.62 because of overlap of the bubbles. Note that because of these overlaps, the shapes of the resulting ionized regions would not always be perfectly spherical. In this scenario, we have essentially attempted to capture a situation where there are many small, possibly overlapping ionized regions produced by galaxies and a few large ionized regions (like the one that we are trying to detect) produced by QSOs.

Since the choice of the background bubble size is not robust by any means, we consider a different scenario PR2 where these bubbles have the same comoving radius R_b as the bubble that we are trying to detect. The centers of these extra bubbles trace the dark matter distribution as in PR1. The number of bubbles is fixed by the globally averaged x_{HI} which we take to be 0.62 same as in PR1. The PR2 scenario represents a situation where we predominantly have large ionized regions produced either by rare luminous sources or through the overlap of several small ionized regions in the later stages of reionization.

A particle-mesh (PM) N-body code was used to simulate the dark matter distribution. Our earlier work (Paper I) shows that the HI signal of the ionized bubble is largely concentrated at small baselines or large angular scales, thus a very high spatial resolution is not required. We have used a grid spacing of 2 Mpc for the simulations. This is adequate for bubbles in the range $4 \leq R_b \leq 50$ Mpc that we consider. The simulations use 256^3 particles on a 256^3 mesh. For the GMRT a single N-body simulation was cut into 8 equal cubes of size 256 Mpc on each side. Considering that each cube may be viewed along three different directions, we have a total of 24 different realization of the dark matter distribution. Each cube corresponds to 18 MHz in frequency and $\sim 2^\circ$ in angle which is comparable to the GMRT FoV which has FWHM=1.7° at 203MHz. The MWA FoV is much larger (FWHM=13°). Here

eight independent N-body simulations were used. Viewing these along three different directions gives twenty four different realizations of the dark matter distribution. Limited computer memory restricts the simulation size and the angular extent ($\sim 4^\circ$) is considerably smaller than the MWA FoV. We do not expect this to affect the signal but the contribution from the HI fluctuations outside the bubble is possibly underestimated for the MWA.

The dark matter density contrast δ was used to calculate the redshifted 21 - cm specific intensity $I_\nu = \bar{I}_\nu x_{\text{HI}} (1 + \delta)$ for each grid point of our simulation. Here $\bar{I}_\nu = 2.5 \times 10^2 \frac{Jy}{sr} \left(\frac{\Omega_b h^2}{0.02} \right) \left(\frac{0.7}{h} \right) \left(\frac{H_0}{H(z)} \right)$ and x_{HI} the hydrogen neutral fraction is 0 inside the ionized bubbles and 1 outside. The simulated boxes are transformed to frequency and sky coordinate. Figure 1 shows the HI image on a slice through the center of the bubble of radius $R_b = 20$ Mpc. The mean neutral fraction \bar{x}_{HI} is ~ 1 in the SB scenario, while it is ~ 0.62 for the two PR simulations shown here.

The three scenarios discussed above consider only spherical bubbles, and the only departures from sphericity arise from bubble overlap. It is important to assess how well our bubble detection technique works for non-spherical bubbles, which we do using ionization maps produced by the semi-numeric (SM) approach. In particular, we use maps obtained by the method of Choudhury, Haehnelt & Regan (2008). Essentially, these maps are produced by incorporating an excursion-set based technique for identifying ionized regions given the density distribution and the ionizing sources (Zahn et al., 2007; Mesinger & Furlanetto, 2007; Geil & Wyithe, 2008). In addition, the method of Choudhury, Haehnelt & Regan (2008) incorporate inhomogeneous recombination and self-shielding of high-density regions so that it is consistent with the “photons-starved” reionization scenario implied by the Ly α forest data (Bolton & Haehnelt, 2007; Choudhury, Ferrara & Gallerani, 2008). We use a simulation box of size 270 Mpc with 2000^3 particles which can resolve collapsed halos as small as $\approx 10^9 M_\odot$. The ionization maps are generated at a much lower resolution with a grid size of 2.7 Mpc. The box corresponds to 19 MHz in frequency and $\sim 2^\circ$ in angle comparable to the GMRT FoV. We have assigned luminosities to the collapsed halos such that the mean neutral fraction $x_{\text{HI}} = 0.5$. The most massive halo (mass $\sim 10^{13} M_\odot$) identified in the box is made to coincide with the box centre and we assume that it hosts a luminous QSO; its luminosity and age

are chosen such that it would produce a spherical HII region of comoving size ≈ 27 Mpc in a completely homogeneous neutral medium [see, e.g., equation (8) of Geil & Wyithe (2008)]. However, the actual ionized region is far from spherical both because of the surrounding bubbles from other halos and also because of inhomogeneous recombination. We find visually from the maps (see the rightmost panel of Figure 1) that the HII region is fully ionized up to radius ≈ 27 Mpc. Beyond that the region is partially filled with neutral patches. This patchy ionized region extends up to radius ~ 42 Mpc and then merges with the average IGM. The fully ionized region and the region with HI patches are marked with two circles. We use this box for GMRT as three independent realizations viewing the box along three different directions. For the MWA we need a much larger simulation box which requires substantially more computing power, beyond the resources available to us at present. Hence we do not consider the MWA for this scenario.

2.1 Simulating Visibilities

The quantity measured in radio-interferometric observations is the visibility $V(\vec{U}, \nu)$ which is related to the specific intensity pattern on the sky $I_\nu(\vec{\theta})$ as

$$V(\vec{U}, \nu) = \int d^2\theta A(\vec{\theta}) I_\nu(\vec{\theta}) e^{2\pi i \vec{\theta} \cdot \vec{U}} \quad (1)$$

Here the baseline $\vec{U} = \vec{d}/\lambda$ denotes the antenna separation \vec{d} projected in the plane perpendicular to the line of sight in units of the observing wavelength λ , $\vec{\theta}$ is a two dimensional vector in the plane of the sky with origin at the center of the FoV, and $A(\vec{\theta})$ is the beam pattern of the individual antenna. For the GMRT this can be well approximated by Gaussian $A(\vec{\theta}) = e^{-\theta^2/\theta_0^2}$ where $\theta_0 \approx 0.6 \theta_{\text{FWHM}}$ and we use the values 1.7° for θ_0 at 203 MHz corresponding to the redshift $z = 6$ for the GMRT. The MWA beam pattern is expected to be quite complicated, and depends on the pointing angle relative to the zenith (Bowman et al., 2007). Our analysis largely deals with the beam pattern within 2° of the pointing angle where it is reasonable to approximate the beam as being circularly symmetric (Figures 3 and 5 of Bowman et al. 2007). We approximate the MWA antenna beam pattern as a Gaussian.

We consider 128 frequency channels across 18MHz bandwidth. The image $I_\nu(\theta)$ at each channel is multiplied with the telescope beam pattern $A(\vec{\theta}, \nu)$. The discrete Fourier transform (DFT) of the product $I_\nu(\theta) A(\vec{\theta}, \nu)$ gives the complex visibilities $\hat{V}(\vec{U}, \nu)$. The GMRT simulations have baselines in the range $30.5 \leq U \leq 3900$ which is adequate to capture the HI signal from ionized bubbles which is expected to be confined to small baselines $U < 1000$.

The visibility recorded in radio-interferometric observations is actually a combination of several contributions

$$V(\vec{U}, \nu) = S(\vec{U}, \nu) + HF(\vec{U}, \nu) + N(\vec{U}, \nu) + F(\vec{U}, \nu). \quad (2)$$

The signal $S(\vec{U}, \nu)$ from an ionized bubble of comoving radius R_b embedded in an uniform HI distribution can be analytically calculated (Paper I). The solid curve in Figures 2 and 3 show the expected signal for $R_b = 20$ Mpc. The U extent, frequency extent and peak value of the signal scale as R_b^{-1} , R_b and R_b^2 respectively for other values of R_b . Note that $S(\vec{U}, \nu)$ is real when the bubble is at the center of the FoV.

The data points shown in Figures 2 and 3 are the real part of a few randomly chosen visibilities determined from the simulation of a $R_b = 20$ Mpc bubble in the SB scenario. The deviations from

the analytic predictions are due to the HI fluctuations $HF(\vec{U}, \nu)$ *ie.* in the SB scenario the HI outside the bubble traces the dark matter fluctuations. Notice that these fluctuations are often so prominent that the signal cannot be made out. We expect even larger fluctuations in the other three scenarios which incorporate patchiness of reionization.

The system noise contribution $N(\vec{U}, \nu)$ in each baseline and frequency channel is expected to be an independent Gaussian random variable with zero mean ($\langle \hat{N} \rangle = 0$) and variance $\sqrt{\langle \hat{N}^2 \rangle}$ is independent of \vec{U} and ν_c . We use (Paper I)

$$\sqrt{\langle \hat{N}^2 \rangle} = C^x \left(\frac{\Delta \nu_c}{1\text{MHz}} \right)^{-1/2} \left(\frac{\Delta t}{1\text{sec}} \right)^{-1/2} \quad (3)$$

where C^x has values 0.53Jy and 54.21Jy for the GMRT and the MWA respectively (Paper I).

The contribution from astrophysical foregrounds $F(\vec{U}, \nu)$ is expected to be several order of magnitude stronger than the HI signal. The foregrounds are predicted to have a featureless, continuum spectra whereas the signal is expected to have a dip at ν_c (Figure 3). This difference holds the promise of allowing us to separate the signal from the foregrounds.

2.2 Simulating Signal Detection

The signal component $S(\vec{U}, \nu)$ in the observed visibilities $V(\vec{U}, \nu)$ is expected to be buried deep in other contributions many of which are orders of magnitude larger. Detecting this is a big challenge. For optimal signal detection we consider the estimator (Paper I)

$$\hat{E} = \sum_{a,b} S_f^*(\vec{U}_a, \nu_b) \hat{V}(\vec{U}_a, \nu_b) \quad (4)$$

where $S_f(\vec{U}, \nu)$ is a filter which has been constructed to detect a particular ionized bubble, $\hat{V}(\vec{U}_a, \nu_b)$ refer to the observed visibilities and \vec{U}_a and ν_b refer to the different baselines and frequency channels in the observation. The filter $S_f(\vec{U}, \nu)$ depends on $[R_f, z_c, \vec{\theta}_c]$ the comoving radius, redshift and angular position of the bubble that we are trying to detect. We do not show this explicitly, the values of these parameters will be clear from the context.

The baselines obtained using DFT in our simulations are uniformly distributed on a plane. In real observations, the baselines will have a complicated distribution depending on the antenna layout and direction of observation. We incorporate this through the normalized baseline distribution function $\rho_N(U, \nu)$ which is defined such that $d^2U d\nu \rho_N(\vec{U}, \nu)$ is the fraction of data points *ie.* baselines and frequency channels in the interval $d^2U d\nu$ and $\int d^2U \int d\nu \rho_N(\vec{U}, \nu) = 1$. We use the functional forms of ρ_N determined in Paper I for the GMRT and the MWA.

Using the simulated visibilities, we evaluate the estimator as

$$\hat{E} = (\Delta U)^2 \Delta \nu \sum_{a,b} S_f^*(\vec{U}_a, \nu_b) \hat{V}(\vec{U}_a, \nu_b) \rho_N(\vec{U}_a, \nu_b) \quad (5)$$

where the sum is now over the baselines and frequency channels in the simulation.

The filter $S_f(\vec{U}, \nu)$ (Filter I of Paper I) is defined as

$$S_f(\vec{U}, \nu) = \left(\frac{\nu}{\nu_c} \right)^2 \left[S(\vec{U}, \nu) - \frac{\Theta(1 - 2|\nu - \nu_c|/B')}{B'} \int_{\nu_c - B'/2}^{\nu_c + B'/2} S(\vec{U}, \nu') d\nu' \right]. \quad (6)$$

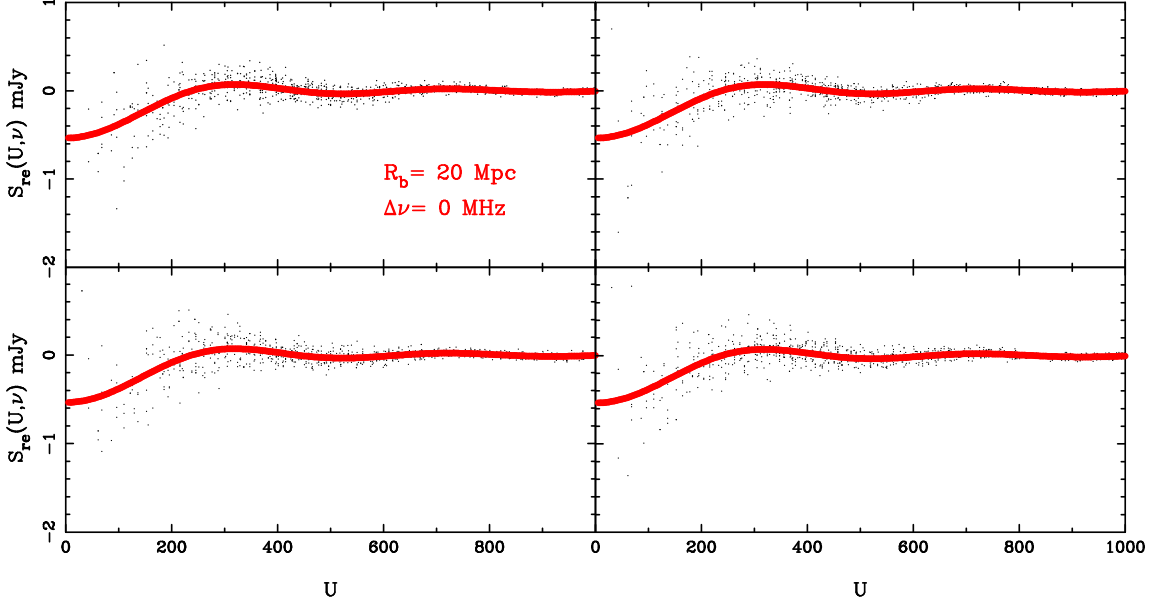


Figure 2. This shows the visibility signal (real part) from a frequency slice through the center of a spherical ionized bubble of comoving radius 20 Mpc embedded in HI. The solid curves show the expected signal assuming that the bubble is embedded in uniformly distributed HI. The data points show the visibilities for a few randomly chosen baselines from our simulation of the SB scenario. The difference between the data points and the solid curve is due to the fluctuations in the HI outside the bubble. Each panel corresponds to a different realization of the simulation.

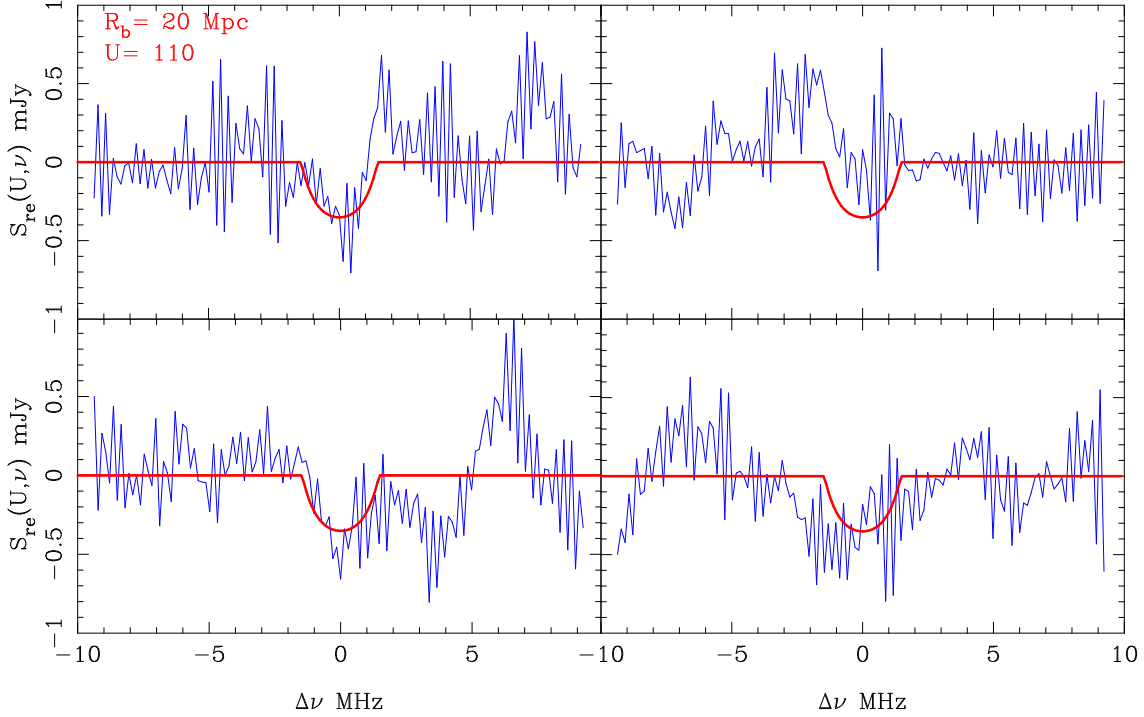


Figure 3. Same as the previous figure except that U is fixed at 110 while the frequency varies, and $\Delta\nu = \nu - \nu_c$.

where the first term $S(\vec{U}, \nu)$ is the expected signal of the bubble that we are trying to detect. We note that this term is the matched filter that gives the maximum signal to noise ratio (SNR). The second term involving the Heaviside function $\Theta(x)$ subtracts out any frequency independent component from the frequency range $\nu_c - B'/2$ to $\nu_c + B'/2$. The latter term is introduced to subtract out the foreground contributions. The $(\nu/\nu_c)^2$ term accounts for

the fact that $\rho_N(U, \nu)$ changes with frequency (equivalently wavelength).

We have used the 24 independent realizations of the simulation for the first three scenarios to determine the mean $\langle \hat{E} \rangle$ and the variance $\langle (\Delta \hat{E})^2 \rangle$ of the estimator. The high computational requirement restricts us to use just 3 realizations for the SM scenario. Only the signal is correlated with the filter, and only this is expected to contribute to the mean $\langle \hat{E} \rangle$. All the other components are uncor-

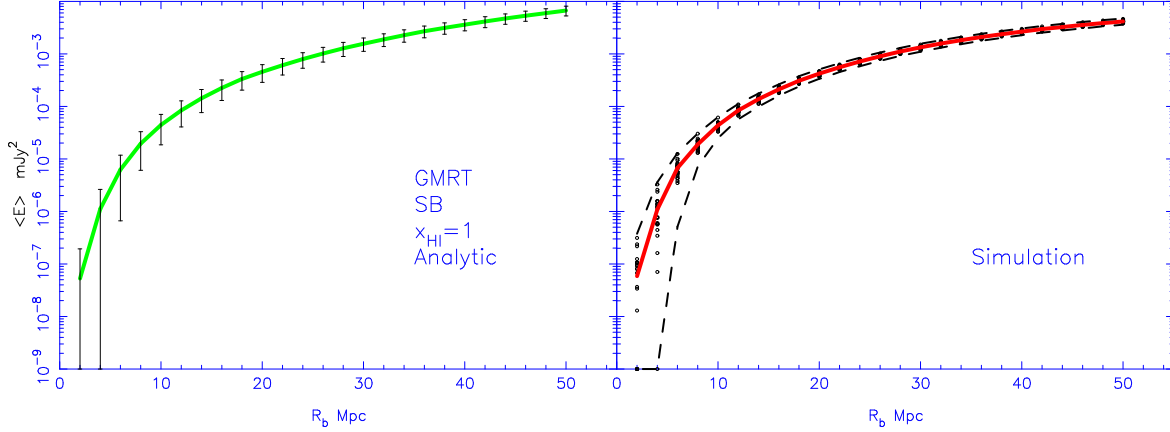


Figure 4. The estimator \hat{E} (defined in equation 4) for bubble size R_b ranging from 4 Mpc to 50 Mpc for the GMRT in the SB scenario. It is assumed that the filter is exactly matched to the bubble. The left panel shows the analytic predictions for the mean estimator $\langle \hat{E} \rangle$ and the $3 - \sigma$ error-bars due to the HI fluctuations. The solid and the dashed lines in the right panel respectively show the $\langle \hat{E} \rangle$ and the $3 - \sigma$ envelope determined from the simulations. The data points in the right panel show \hat{E} in the individual realizations.

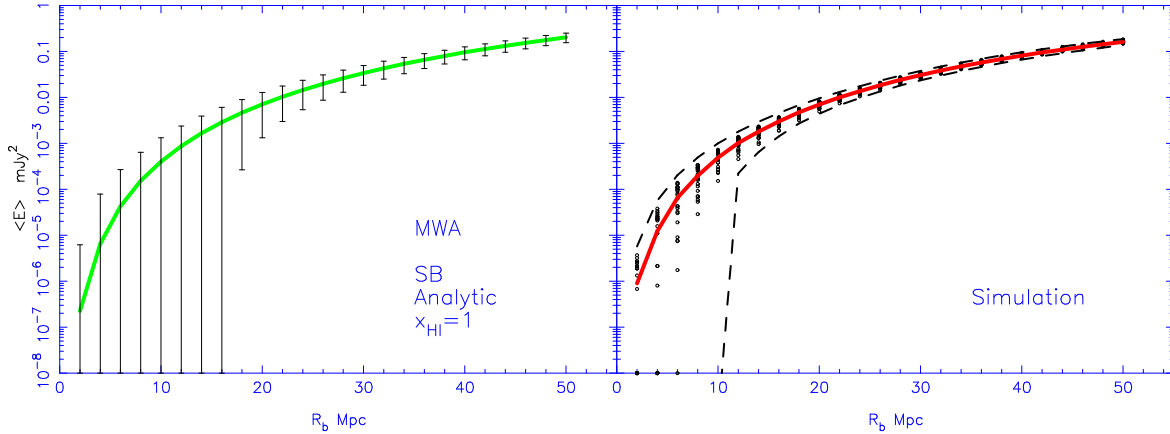


Figure 5. Same as the Figure 4 for the MWA.

related with the filter and they are expected to contribute only to the variance $\langle (\Delta \hat{E})^2 \rangle$. The variance is a sum of three contributions (Paper I)

$$\langle (\Delta \hat{E})^2 \rangle = \langle (\Delta \hat{E})^2 \rangle_{HF} + \langle (\Delta \hat{E})^2 \rangle_N + \langle (\Delta \hat{E})^2 \rangle_{FG}. \quad (7)$$

The simulations give an estimate of $\langle (\Delta \hat{E})^2 \rangle_{HF}$ the contribution from HI fluctuations. We do not include system noise explicitly in our simulations. The noise contribution from a single visibility (eq. 3) is used to estimate $\langle (\Delta \hat{E})^2 \rangle_N$ (eq. 19 of Paper I). Under the assumed foreground model, the foreground contribution $\langle (\Delta \hat{E})^2 \rangle_{FG}$ is predicted to be smaller than the signal and we do not consider it here.

3 RESULTS

We first consider the detection of an ionized bubbles and the estimation of its parameters in the SB scenario where there is only a single bubble in the FoV. We consider the most optimistic situation where the bubble is located in the center. In reality this can only be achieved in targeted observations of ionized bubbles around luminous QSOs. In a blind search, the bubble in general will be located at some arbitrary position in the FoV, and not the center. It has already been mentioned that the foregrounds can be removed

by a suitable choice of the filter. Further, the system noise can, in principle, be reduced by increasing the observation time. The HI fluctuations outside the bubble impose a fundamental restriction on bubble detection.

3.1 Restriction on bubble detection

We have carried out simulations for different values of the bubble radius R_b chosen uniformly at an interval of 2 Mpc in the range 4 to 50 Mpc. In each case we consider only the most optimistic situation where the bubble radius R_f used in the filter is precisely matched to R_b . In reality it is necessary to try filters of different radius R_f to determine which gives the best match.

Figures 4 and 5 shows the results for the GMRT and the MWA respectively. We compare the analytic predictions of Paper I (left panel) with the prediction of our simulations (right panel). The analytical predictions for the mean value $\langle \hat{E} \rangle$ arising from the signal and $\sqrt{\langle (\Delta \hat{E})^2 \rangle_{HF}}$ due to the HI fluctuations are respectively calculated using equations (15) and (22) of Paper I. The signal depends on the bubble radius R_b and the mean neutral fraction which is taken to be $x_{\text{HI}} = 1$. The uncertainty due to the HI fluctuations is calculated using the dark matter power spectrum under the assumption that the HI traces the dark matter.

We find that $\langle \hat{E} \rangle$ and $\sqrt{\langle (\Delta \hat{E})^2 \rangle_{HF}}$ determined from the simulations is in rough agreement with the analytic predictions. The mean $\langle \hat{E} \rangle$ is in very good agreement for $R_b > 6$ Mpc, there is a slight discrepancy for smaller bubbles arising from the finite grid size (2 Mpc in the simulation). The HI fluctuations $\sqrt{\langle (\Delta \hat{E})^2 \rangle_{HF}}$ are somewhat underestimated by the simulations. This is more pronounced for the MWA where the limited box size of our simulations results in a FoV which is considerably smaller than the actual antennas. We note that the 24 different values of \hat{E} determined from the different realizations of the simulation all lie within $\langle \hat{E} \rangle \pm 3\sqrt{\langle (\Delta \hat{E})^2 \rangle_{HF}}$ determined from the analytic predictions.

The good agreement between the simulation results and the analytical predictions is particularly important because each is based on several approximations, many of which differ between the two methods. Our results show that the effect of these approximations, though present, are well under control. The analytical method has the advantage that it is very easy to calculate and can be evaluated very quickly at an extremely low computational cost. Unfortunately, its utility is mainly limited to the SB scenario and it cannot be easily applied to an arbitrary PR scenario with a complicated HI distribution. Simulations, though computationally more cumbersome and expensive, are useful in such a situation. It is thus important to test that the two methods agree for the SB scenario where both of them can be applied. Note that the HI fluctuation predicted by the SB scenario sets the lower limit for the HI fluctuation in any of the PR models. It is expected that patchiness will increase the HI fluctuations above the SB predictions.

It is meaningful to attempt bubble detection at, say 3σ confidence level, only if $\langle \hat{E} \rangle \geq 3\sqrt{\langle (\Delta \hat{E})^2 \rangle_{HF}}$. The HI fluctuations overwhelm the signal in a situation where this condition is not satisfied, and bubble detection is not possible. In a situation where this condition is satisfied, an observed value E_o of the estimator can be interpreted as a 3σ detection if $E_o > 3\sqrt{\langle (\Delta \hat{E})^2 \rangle}$. The simulations show that a $3 - \sigma$ detection is not possible for $R_b \leq 6$ Mpc and $R_b \leq 12$ Mpc at the GMRT and MWA respectively. As noted earlier, the HI fluctuations are somewhat under-predicted in the simulations and the analytic predictions $R_b \leq 8$ Mpc and $R_b \leq 16$ Mpc respectively, are somewhat larger.

The limitation on the bubble size R_b that can be detected is larger for the MWA as compared to the GMRT. This is because of two reasons, the first being the fact that the MWA has a very dense sampling of the small baselines where the HI fluctuation are very large, and the second being the large FoV. In fact, the baseline distribution of the experiment has a significant role in determining the quantum of HI fluctuations and thereby determining the lower cut-off for bubble detection. Looking for an optimum baseline distribution for bubble detection is also an issue which we plan to address in future. In a situation where the antenna layout is already in place, it may be possible to tune the filter to reduce the HI fluctuations.

We have not considered the effect of peculiar velocities (Bharadwaj & Ali, 2004) in our simulations. From equation (22) of Paper I we see that the HI fluctuations scale as $\sqrt{\langle (\Delta \hat{E})^2 \rangle_{HF}} \propto \sqrt{C_l}$, where C_l is the HI multi-frequency angular power spectrum (MAPS). The C_l s increase by a factor ~ 2 due to peculiar velocities, whereby $\sqrt{\langle (\Delta \hat{E})^2 \rangle_{HF}}$ goes up by a factor ~ 1.5 . This increase does not significantly change our results, and is small compared to the other uncertainties in the PR models.

The signal $\langle \hat{E} \rangle$ and the HI fluctuations $\sqrt{\langle (\Delta \hat{E})^2 \rangle_{HF}}$ both

scale as $\propto \bar{x}_{HI}$, and the lower limit for bubble detection is unchanged for smaller neutral fractions.

3.2 Size Determination

In this subsection we estimate the accuracy to which it will be possible to determine the bubble radius R_b . This, in general, is an unknown quantity that has to be determined from the observation by trying out filters with different values of R_f . In the matched filter technique we expect the predicted SNR (only system noise) ratio

$$\text{SNR} = \frac{\langle \hat{E} \rangle}{\sqrt{\langle (\Delta \hat{E})^2 \rangle_{\text{NS}}}} \quad (8)$$

to peak when the filter is exactly matched to the signal *ie.* $R_f = R_b$. The solid line in the right panel of Figure 6 shows this for $R_b = 10$ Mpc. We find that the SNR peaks exactly when the filter size $R_f = 10$ Mpc. We propose that this can be used to observationally determine R_b . For varying R_f , we consider the ratio of the observed value E_o to the expected system noise $\sqrt{\langle (\Delta \hat{E})^2 \rangle_{\text{NS}}}$, referring to this as the SNR. The R_f value where this SNR peaks gives an estimate of the actual bubble size R_b . The observed SNR will differ from the predictions of eq. (8) due to the HI fluctuations outside the bubble. These variations will differ from realization to realization and this can introduce uncertainties in size estimation. We have used the simulations to estimate this.

The left panel of Figure 6 shows the SNR as a function of R_f for 4 different realizations of the simulation for the GMRT with bubble size $R_b = 10$ Mpc. We see that for $R_f \leq R_b$ the SNR shows a very similar behavior in all the realizations, and it always peaks around 10 Mpc as expected. For $R_f > R_b$ the behavior of the SNR as a function of R_f shows considerable variation across the realizations. In some cases the drop in SNR away from the peak is quite rapid whereas in others it is very gradual (for example, the dashed-dot-dot curve). In many cases there is a spurious extra peak in the SNR at an R_f value that is much larger than R_b . These spurious peaks do not pose a problem for size determination as they are well separated from R_b and can be easily distinguished from the genuine peak.

The error-bars in the right panel of Figure 6 show the $3 - \sigma$ fluctuation in the simulated SNR determined from 24 realizations of the simulation. Note that the fluctuations at different R_f are correlated. Although the overall amplitude changes from one realization to another, the shape of the curve in the vicinity of $R_f = R_b$ is nearly invariant across all the realizations. In all of the 24 realizations we can identify a well defined peak at the expected value $R_f = R_b$.

Figures 7 and 8 show the results for a similar analysis with $R_b = 20$ Mpc for the GMRT and the MWA respectively. It is not possible to detect a bubble of size $R_b = 10$ Mpc with the MWA, and hence we do not show this. Here again, we find that for all the realizations of the simulations the SNR peaks at $R_f = R_b$. The relative variations in the SNR across the realizations is much less for $R_b = 20$ Mpc as compared to 10 Mpc and there are no spurious peaks. Also, for the same bubble size the variations are smaller for the GMRT as compared to the MWA. We do not find any spurious peaks for $R_b = 20$ Mpc.

A point to note is that the mean SNR determined from the simulations is somewhat smaller than the analytic predictions, both being shown in the right panels of Figures 6, 7 and Figure 8. There are a couple of reasons that could account for this namely, (i) the bubble in the simulation is not exactly a sphere because of the finite

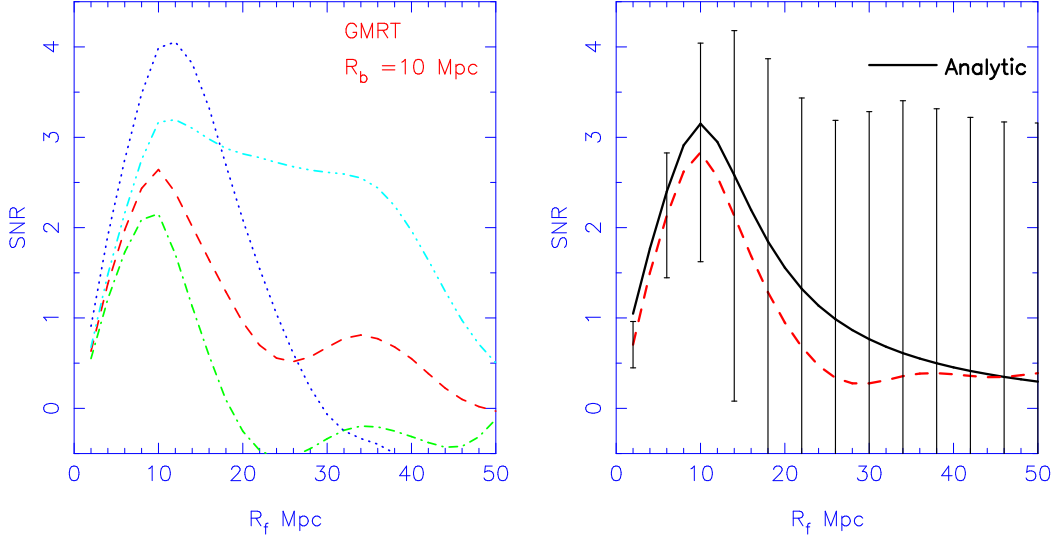


Figure 6. The $\text{SNR} = \langle \hat{E} \rangle / \sqrt{\langle (\Delta \hat{E})^2 \rangle_{\text{NS}}}$ for 1000 hrs observation with the GMRT as a function of the filter size R_f for the case where the actual bubble size is $R_b = 10$ Mpc. The left panel shows 4 different realizations of the simulation. The right panel shows the mean SNR and $3-\sigma$ error-bars calculated using 24 realizations. The solid line shows the analytical predictions.

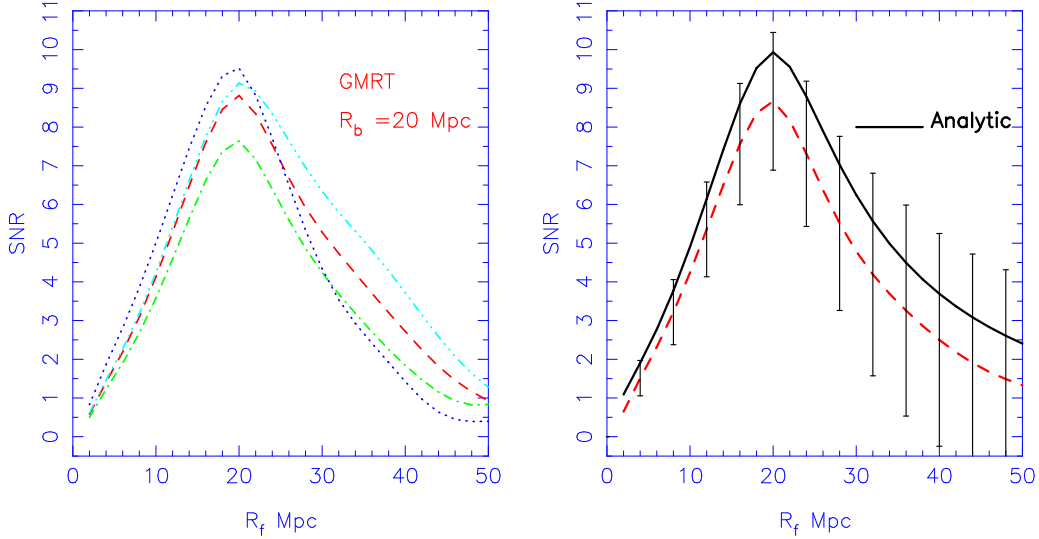


Figure 7. Same as the Figure 6 for $R_b = 20$ Mpc for the GMRT.

grid size and thus the match between the filter and the signal is not perfect even when the sizes are same and (ii) the finite box-size imposes a minimum baseline beyond which the signal is not represented in the simulation.

Based on our results we conclude that in the SB scenario for the GMRT the accuracy to which the bubble size can be determined in our simulations is decided by the resolution 2 Mpc and not by the HI fluctuations. In reality the limitation will come from the angular resolution of the instrument which sets the limit at 0.5 Mpc for the GMRT and 8 Mpc for the MWA.

The height of the SNR peak depends on the neutral fraction and it can be used to observationally determine this. We find that the HI fluctuations do not change the position of the peak but introduce considerable variations in its height even if $x_{\text{HI}} = 1$. The HI fluctuations restrict the accuracy to which the neutral fraction can be estimated, an issue that we propose to address in future work.

3.3 Determining the position

In the previous two subsections, we have considered cases where the bubble's position is known. Here we assume that the bubble's size is known and we estimate the accuracy to which its position can be determined in the presence of HI fluctuations. The situation considered here is a blind search whereas the former is a targeted search centered on a QSO.

In a real situations it would be necessary to jointly determine four parameters the bubble radius R_b , two angular coordinates (θ_x, θ_y) and the central frequency ν_c from the observation. However, to keep the computational requirement under control, in this analysis we assume that R_b is known. The bubble is placed at the center of the FoV and frequency band, and we estimate how well the position can be recovered from the simulation. To determine the bubble's position we move the center of the filter to different positions and search for a peak in the SNR. To reduce the com-

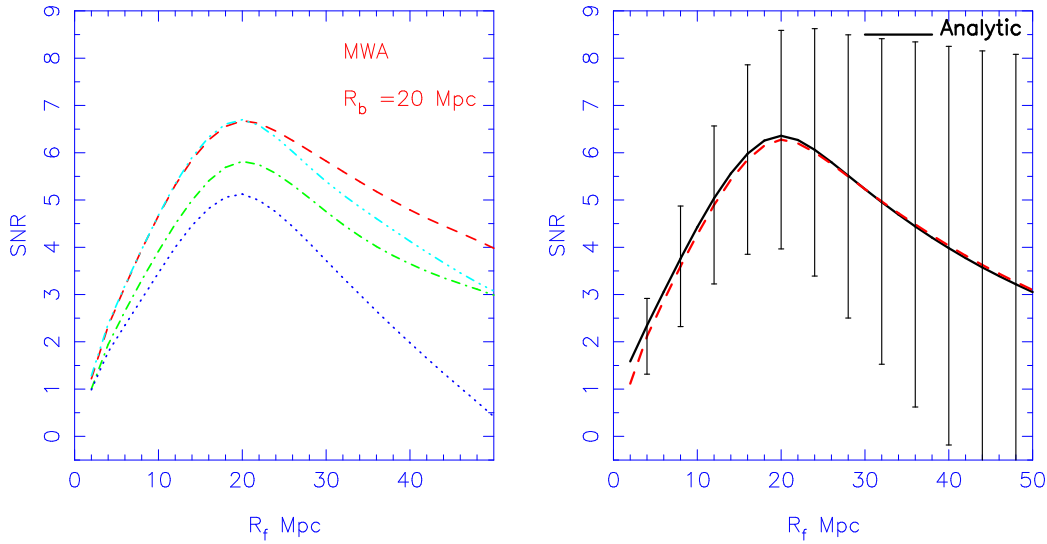


Figure 8. Same as the Figure 6 for $R_b = 20$ Mpc for the MWA.

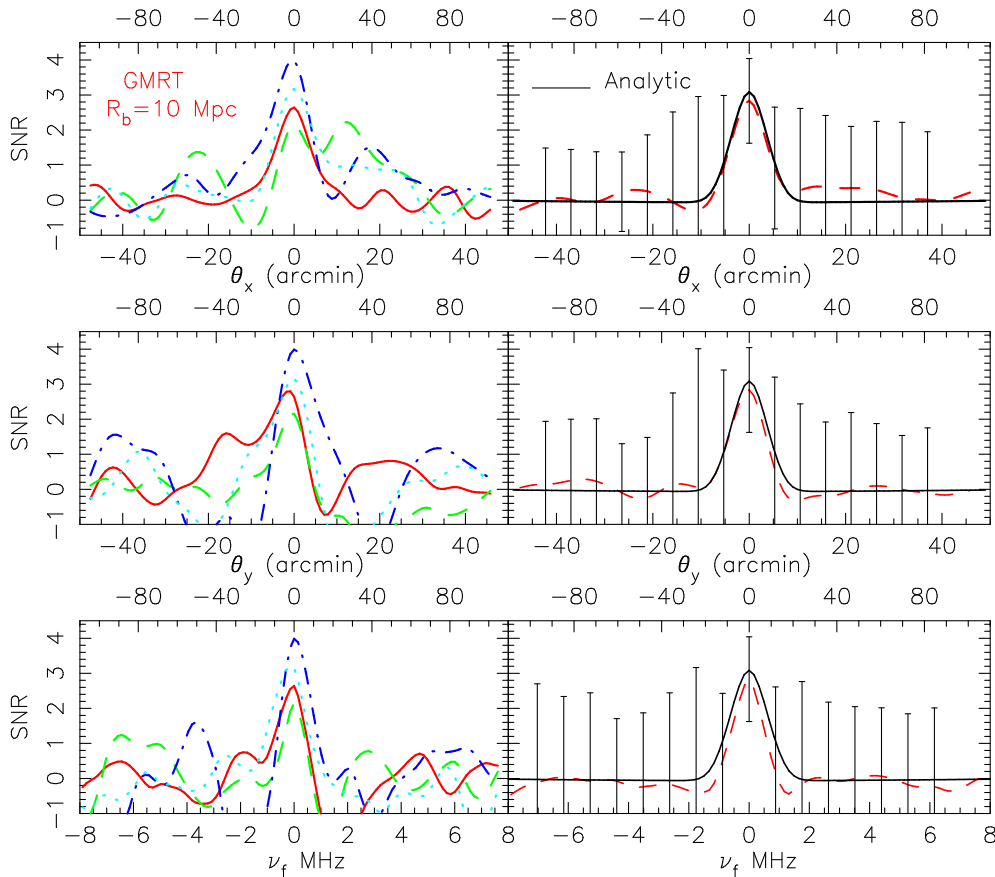


Figure 9. The SNR for 1000 hrs GMRT observations for a bubble of size $R_b = 10$ Mpc located at the center of the field of view. The filter scans along $\theta_x, \theta_y, \nu_f$ (top, middle, bottom) to determine the bubble's position. The left panel shows results for 4 realizations of the SB simulation, the right panels show the mean (dashed curve) and $3 - \sigma$ error-bars determined from 24 realizations of the simulation and the analytic prediction for the mean (solid curve).

computational requirement, this is done along one direction at a time, keeping the other two directions fixed at the bubble's actual center. We have also carried out simulations where the bubble is located off-center. We do not explicitly show these results because they are exactly the same as when the bubble is at the center except for the

fact that the value of the peak SNR is lower because of the primary beam pattern.

Figure 9 shows the results for $R_b = 10$ Mpc for the GMRT. The left panel shows results for 4 realizations of the simulation, the right panels show the mean and $3 - \sigma$ determined from 24 realizations of the simulations and the analytic prediction for the

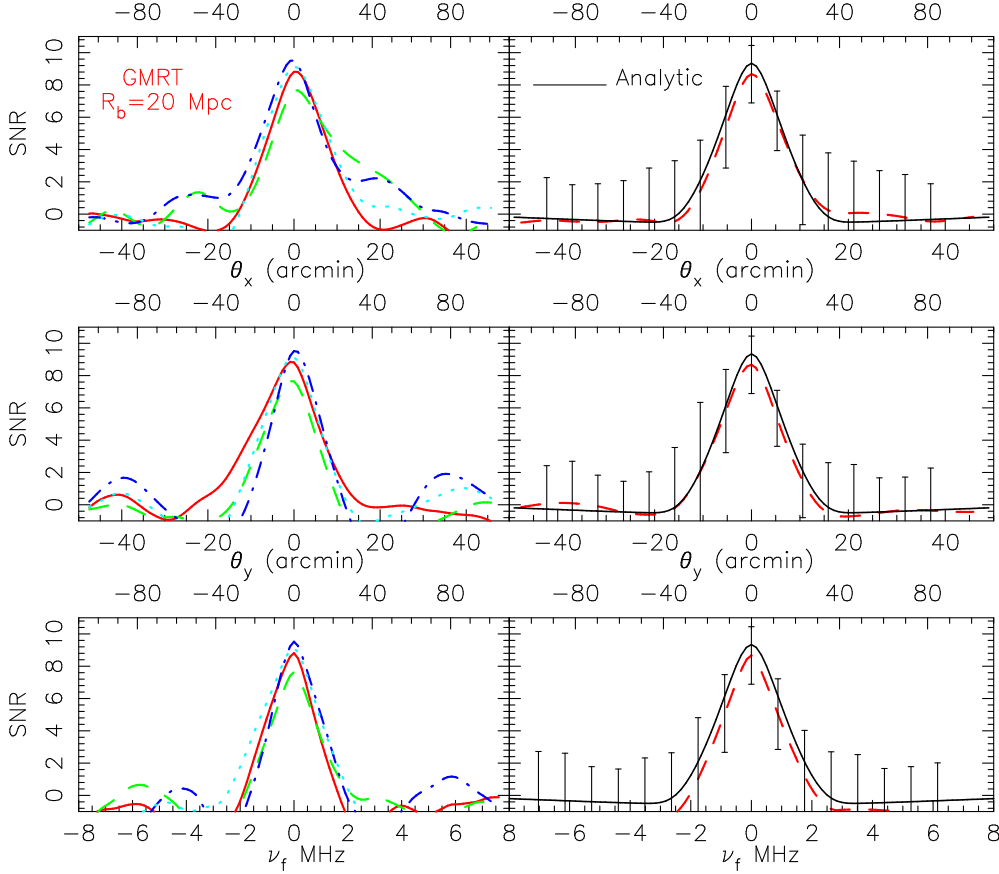


Figure 10. Same as the Figure 9 for $R_b = 20$ Mpc for the GMRT.

mean value. In all cases a peak is seen at the expected position matched with the bubble’s actual center. The HI fluctuations pose a severe problem for determining the bubble’s position as it introduces considerable fluctuations in the SNR. In some cases these fluctuations are comparable to the peak at the bubble’s actual position (see the dashed line in the upper left panel). The possibility of spurious peaks makes it difficult to reliably determine the bubble’s position.

We present the results for $R_b = 20$ Mpc in Figures 10 and 11 for the GMRT and MWA respectively. The HI fluctuations do not pose a problem for determining the position of such bubbles using the GMRT. In all the realizations of the GMRT simulations there is a peak at the expected position. The FWHM ~ 40 Mpc is approximately the same along θ_x, θ_y and ν_f and is comparable to the separation at which the overlap between the bubble and the filter falls to half the maximum value. The HI fluctuations does introduce spurious peaks, but these are quite separated from the actual peak and have a smaller height. We do not expect these to be of concern for position estimation.

The MWA simulations all show a peak at the expected bubble position. The FWHM along θ (~ 60 Mpc) is somewhat broader than that along ν (~ 40 Mpc). The low spatial resolution ~ 8 Mpc possibly contributes to increase the FWHM along θ . The HI fluctuations introduce spurious peaks whose heights are $\sim 50\%$ of the height of the actual peak.

3.4 Bubble Detection in Patchy Reionization

The SB scenario considered till now is the most optimistic scenario in which the HI traces the dark matter. The presence of ionized patches other than the one that we are trying to detect is expected to increase the contribution from HI fluctuations. We first consider the PR1 scenario where there are several additional ionized bubbles of radius 6 Mpc in the FoV. Figures 12 & 13 show the mean value of the estimator $\langle \hat{E} \rangle$ and $3 - \sigma$ error-bars as a function of R_f for the GMRT and the MWA respectively. These were estimated from 24 different realizations of the simulation, using a filter exactly matched to the bubble.

We find that the results are very similar to those for the SB scenario except that the signal is down by 0.6 due to the lower neutral fraction ($x_{\text{HI}} = 0.62$) in the PR scenarios. Ionized bubbles with radius $R_b = 8$ Mpc and $= 12$ Mpc or smaller cannot be detected by the GMRT and MWA respectively due to the HI fluctuations. These limits are similar to those obtained in simulations of the SB scenario.

In the PR2 scenario the FoV contains other ionized bubbles of the same size as the bubble that we are trying to detect. We find that bubble detection is not possible in such a situation, the HI fluctuations always overwhelm the signal. This result obviously depends on number of other bubbles in the FoV, and this is decided by x_{HI} which we take to be 0.62. A detection may be possible at higher x_{HI} where there would be fewer bubbles in the FoV.

In the SM scenario, the very large computation time restricts us from generating several realizations with central ionized regions of different sizes. Hence we are unable to study the restriction on

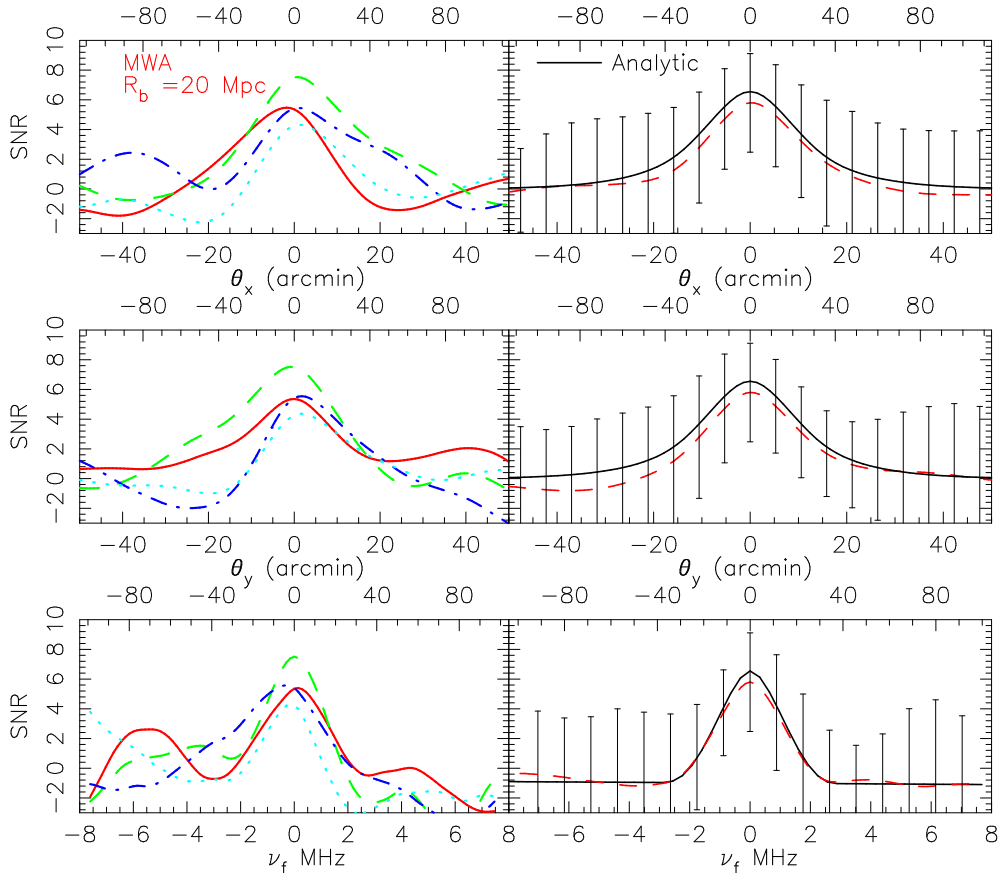


Figure 11. Same as the Figure 9 for $R_b = 20$ Mpc for the MWA.

bubble detection. We have only three realizations all of which have the same ionized region located at the center of the box. Based on these we find that the mean estimator $\langle \hat{E} \rangle$ is ~ 30 times larger than the standard deviation due to HI fluctuations. The detection of a bubble of the size present in our simulation (Figure 1) is not restricted by the HI fluctuations. We present size determination results in Figure 14. We see that the SNR peaks at $R_f = 42$ Mpc and not at $R_f = 27$ Mpc. Recall that in the 21-cm map (Figure 1) we have visually identified the former as the bubble's outer radius which includes several small patchy ionized regions towards the periphery and the latter is the inner radius which encloses the completely ionized region. We see that the matched filter identifies the bubble's outer radius. To study the effect of non-sphericity we compare our results in Figure 14 with the predictions for a spherical bubble of radius $R_b = 42$ Mpc embedded in uniform HI with the same neutral fraction $x_{\text{HI}} = 0.5$. We find that our results for the SM scenario follow the spherical bubble prediction up to a filter size $R_f = 28$ Mpc (marked with a vertical line in Figure 14), corresponding to the bubble's inner radius which encloses a perfectly spherical ionized region. Beyond this, and upto the outer radius of 42 Mpc, the HI is not fully ionized. There are neutral patches which introduce deviations from spherical symmetry and cause the SNR to fall below the predictions of a spherical bubble beyond $R_f = 28$ Mpc. The deviations from sphericity also broadens the peak in the SNR relative to the predictions for a spherical bubble.

Our results based on the SM scenario show that the matched filter technique works well for bubble detection and for determining the bubble's size even when there are deviations from sphericity. We obtain good estimates for the extents of both, the completely

ionized region and the partially ionized region. For the SM scenario, Figure 15 shows how well the bubble's position can be determined in a blind search. We have followed the same method as described for the SB scenario in subsection 3.3. We see that the SNR peaks at the expected position. Further, as the bubble size is quite large $\gtrsim 27$ Mpc there are no spurious peaks.

4 REDSHIFT DEPENDENCE

Results shown so far are all at only one redshift $z = 6$. It would be interesting and useful to have predictions for higher redshifts. However, addressing this issue through direct computations at different redshifts would require considerable computation beyond the scope of this work. Since we find that the analytic predictions of Paper I are in good agreement with the simulations of the SB scenario, we use the analytic formalism to predict how different quantities are expected to scale with increasing z .

The redshift dependence of some of the quantities like the system noise, the background 21-cm brightness \bar{I}_ν , and the angular and frequency extent of a bubble of fixed comoving radius causes the SNR to decrease with increasing z . On the other hand the z dependence of the neutral fraction, the baseline distribution function and the effective antenna collecting area acts to increase the SNR at higher redshifts. We find that with increasing z both $\langle \hat{E} \rangle$ and $\sqrt{\langle (\Delta \hat{E})^2 \rangle_{\text{HF}}}$ decrease by nearly the same factor so that the restriction on bubble detection does not change significantly at higher redshift in the SB scenario. Assuming that the neutral fraction does not change with z , the SNR for bubble detection decreases with

increasing redshift, the change depending on the bubble size. For example, for the GMRT at $z = 10$ the SNR decreases by a factor ~ 7 and 6 for bubbles of size $R_b = 10$ and 20 Mpc respectively. For the MWA this factor is 3 for both these bubble sizes. We expect a similar change in the SNR for the patchy reionization scenarios. The drop in SNR is slower for the MWA relative to the GMRT because the effective antenna collecting area of the MWA increases at higher redshifts.

The SNR is directly proportional to the global neutral fraction x_{HI} which increases with z . The details of how x_{HI} and the HI fluctuations change with redshift depends on how reionization proceeds with time, an issue beyond the scope of this paper.

5 SUMMARY

We have used a visibility-based formalism, introduced in Datta, Bharadwaj & Choudhury (2007), to simulate the detection of spherical HII bubbles in redshifted 21 cm maps through a matched-filtering technique. The main aim of this work is to use simulations to quantify the limitations for bubble detection arising from the HI fluctuations outside the bubble. We have computed the results for two instruments, namely, the GMRT and the upcoming MWA. Our main conclusions are as follows:

- In the case where the HI fluctuations outside the bubble trace the dark matter distribution (SB scenario), we find that bubbles with radius $R_b = 6$ Mpc and $= 12$ Mpc or smaller cannot be detected by the GMRT and MWA respectively due to the HI fluctuations. Note that this limitation is fundamental to the observations and cannot be improved upon by increasing integration time.

- For targeted observations of ionized bubbles, the bubble size can be determined to an accuracy limited by the instrument’s resolution; we find that HI fluctuations do not play any significant role. However, the HI fluctuations can restrict the accuracy to which the neutral fraction can be estimated. In addition, we find that determining the position of the bubble in a blind search could be quite difficult for small (~ 10 Mpc) bubbles as the HI fluctuations introduce large fluctuations in the signal; for larger bubbles the accuracy is determined by the instrument’s resolution.

- In a scenario of patchy reionization where the targeted HII region is surrounded by many small ionized regions of size ~ 6 Mpc (PR1 scenario), the lower limit for bubble detection is similar to that in the SB scenario. Thus the assumption that the HI traces the dark matter gives a reasonable estimate of the contribution from HI fluctuations if the background ionized bubbles are small ~ 6 Mpc. However, the situation is quite different when the surrounding bubbles are of similar size as the targeted bubble (PR2 scenario). The large HI fluctuations do not permit bubble detection for a neutral fraction $x_{\text{HI}} < 0.6$. Thus for $x_{\text{HI}} = 0.6$ or lower, bubble detection is possible only if the other ionized regions in the FoV are much smaller than the bubble that we are trying to detect.

- The matched filter technique works well for more realistic cases based on the semi-numeric modelling of ionized regions (Choudhury, Haehnelt & Regan, 2008). Here the bubbles are substantially non-spherical because of surrounding bubbles and inhomogeneous recombination. Our method gives a good estimate of the size of both the fully ionized and the partially ionized regions in the bubble.

To put our conclusions in an overall perspective, let us consider an ionized bubble around a luminous QSO at $z \gtrsim 6$. We expect $R_b \gtrsim 30$ Mpc from studies of QSO absorption spectra (Wyithe

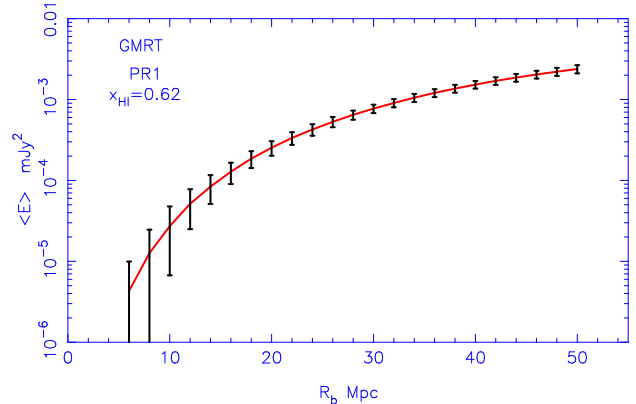


Figure 12. The mean $\langle \hat{E} \rangle$ and $3-\sigma$ error-bars of the estimator as a function of R_b for the GMRT estimated from 24 different realizations of the PR1 scenario. In all cases the filter is exactly matched to the bubble.

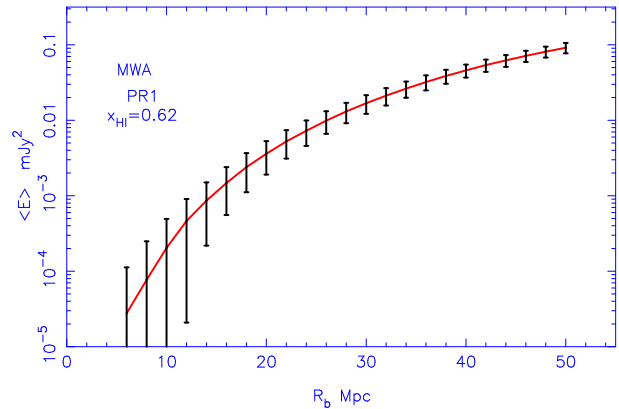


Figure 13. Same as the Figure 12 for the MWA.

& Loeb 2004b; Mesinger & Haiman 2004). It has also been pointed out that these bubbles may survive as large “gray fossils” a long time after the source has shut down (Furlanetto et al. 2008). It will be possible to detect such bubbles only if the background bubbles are smaller, say, < 30 Mpc. We find from models of Mesinger & Furlanetto (2007) that the typical sizes of ionized regions when $x_{\text{HI}} \sim 0.3(0.1)$ is $\sim 20(70)$ Mpc. Though these values could be highly model-dependent, it still gives us an idea that the bubbles around the luminous QSO would be detectable even in a highly ionized IGM with, say, $x_{\text{HI}} \sim 0.3$. If the size of the targeted bubble is larger, then this constraint is less severe. This gives a realistic hope of detecting these bubbles at $z \gtrsim 6$ with near-future facilities.

A caveat underlying a large part of our analysis is the assumption that the bubbles under consideration are perfectly spherical. This is not the case in reality. For example, non-isotropic emission from the sources (QSOs), density fluctuations in the IGM and radiative transfer effects would distort the shape of the bubble. The semi-numeric simulations (SM scenario) incorporate some of these effects and give an estimate of the impact of the deviations from sphericity on bubble detection. This is an important issue which we plan to address in more detail in future. In addition, the finite light travel time gives rise to an apparent non-sphericity even if the physical shape is spherical (Wyithe & Loeb, 2004a; Yu, 2005). This effect can, in principle, be estimated analytically and incorporated in the filter. We plan to address this effect in a separate publication.

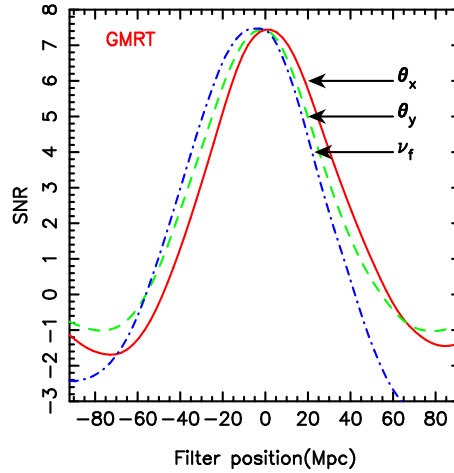


Figure 15. Same as Figure 9 for the SM scenario for the GMRT. The x-axis shows the comoving distance of the filter position from the center of the box. The three curves respectively show results for a search along three θ_x , θ_y and ν axes.

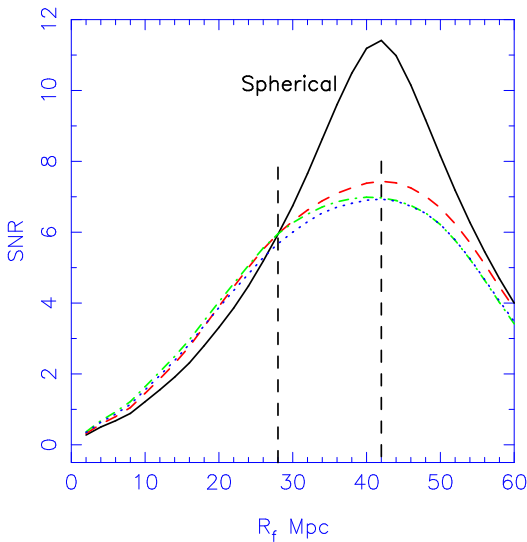


Figure 14. Same as Figure 6 for the SM scenario for the GMRT. The dotted, dashed dotted and dashed lines show results for three different realizations. To show the effect of non-sphericity, we compare these results with predictions for a spherical bubble of sized $R_b = 42$ Mpc embedded in uniform HI with neutral fraction $x_{\text{HI}} = 0.5$ (solid line). The vertical line at $R_f = 28$ Mpc shows the radius up to which the bubble is fully ionized and the SNR follows the spherical predictions. The SNR peaks at $R_f = 42$ Mpc marked by another vertical line.

6 ACKNOWLEDGMENT

We would like to thank M. Haehnelt and J. Regan for allowing us to use the ionization maps of Choudhury, Haehnelt & Regan (2008). KKD and SM would like to thank Prasun Dutta and Prakash Sarkar for useful discussions. KKD is supported by a senior research fellowship of Council of Scientific and Industrial Research (CSIR), India.

References

- Ali, S. S., Bharadwaj, S., & Pandey, B. 2005, MNRAS, 363, 251
 Ali, S. S., Bharadwaj, S., & Chengalur, J. N. 2008, MNRAS, 385, 2166
 Alvarez, M. A., & Abel, T. 2007, MNRAS, 380, L30
 Becker, R.H., et al., 2001, AJ, 122, 2850
 Bharadwaj, S., & Ali, S. S. 2004, MNRAS, 352, 142
 Bharadwaj, S., & Ali, S. S. 2005, MNRAS, 356, 1519
 Bolton, J. S., & Haehnelt, M. G., 2007, MNRAS, 382, 325
 Bowman, J. D., et al. 2007, AJ, 133, 1505
 Choudhury, T. R., Ferrara, A., 2006, Cosmic Polarization, Editor - R. Fabbri (Research Signpost), p. 205, arXiv:astro-ph/0603149
 Choudhury, T. R., Ferrara, A., & Gallerani, S., 2008, MNRAS, 385, L58
 Choudhury, T. R., Haehnelt, M. G., & Regan, J. 2008, ArXiv e-prints, 806, arXiv:0806.1524
 Cooray, A., & Furlanetto, S. R. 2004, ApJL, 606, L5
 Datta, K. K., Choudhury, T. R., & Bharadwaj, S. 2007, MNRAS, 378, 119
 Datta, K. K., Bharadwaj, S., & Choudhury, T. R., 2007, MNRAS, 382, 109
 Di Matteo, T., Perna, R., Abel, T., & Rees, M. J. 2002, ApJ, 564, 576
 Dunkley, J., et al. 2008, arXiv:astro-ph/0803.0586
 Fan, X., et al. 2002, AJ, 123, 1247
 Fan, X., et al. 2006a, AJ, 132, 117
 Fan, X., Carilli, C. L., & Keating, B., 2006, Annual Review of Astronomy & Astrophysics, 44, 415
 Furlanetto, S. R., McQuinn, M., & Hernquist, L. 2006, MNRAS, 365, 115
 Furlanetto, S., Haiman, Z., & Oh, S. P. 2008, arXiv:astro-ph/0803.3454
 Geil, P. M., & Wyithe, J. S. B. 2008, MNRAS, 386, 1683
 Geil, P. M., Wyithe, S., Petrovic, N., & Oh, P. 2008, arXiv:astro-ph/0805.0038
 Gleser, L., Nusser, A., & Benson, A. J. 2007, arXiv:astro-ph/0712.0497
 Kohler, K., Gnedin, N. Y., Miralda-Escudé, J., & Shaver, P. A. 2005, ApJ, 633, 552
 Maselli, A., Gallerani, S., Ferrara, A. & Choudhury, T. R. 2007, MNRAS, 376, L34
 Mesinger, A., & Furlanetto, S. 2007, ApJ, 669, 663
 Mesinger, A., & Haiman, Z. 2004, ApJ, 611, L69
 Morales, M. F., & Hewitt, J. 2004, ApJ, 615, 7
 Oh, S. P., & Mack, K. J. 2003, MNRAS, 346, 871

- Page, L. et al., 2007, *ApJS*, 170, 335
Santos, M. G., Cooray, A., & Knox, L. 2005, *ApJ*, 625, 575
Sethi, S. K. 2005, *MNRAS*, 363, 818
Shaver, P. A., Windhorst, R. A., Madau, P., & de Bruyn, A. G. 1999, *AA*, 345, 380
Spergel, D. N., et al. 2007, *ApJS*, 170, 377
Swarup G., Ananthkrishnan S., Kapahi V.K., Rao A.P., Subramanya C.R., Kulkarni V.K., 1991 *Curr.Sci.*, 60, 95
Wyithe, J. S. B., & Loeb, A. 2004a, *ApJ*, 610, 117
Wyithe, J. S. B., & Loeb, A. 2004b, *Nature*, 432, 194
Wyithe, J. S. B., Loeb, A., & Barnes, D. G. 2005, *ApJ*, 634, 715
Wyithe, J. S. B. 2008, *MNRAS*, 387, 469
Yu, Q. 2005, *ApJ*, 623, 683
Zahn, O., Lidz, A., McQuinn, M., Dutta, S., Hernquist, L., Zal-darriaga, M., & Furlanetto, S. R. 2007, *ApJ*, 654, 12
Zaldarriaga, M., Furlanetto, S. R., & Hernquist, L. 2004, *ApJ*, 608, 622